

Article

Genesis of Pyrite Concretions: Constraints from Mineral and Geochemical Features of Longtan Formation in Anhui Province, Eastern China

Qing He ¹, Yanfei An ^{1,*} , Fangji Sun ² and Chunkit Lai ^{3,4} ¹ School of Resources and Environmental Engineering, Anhui University, Hefei 230601, China² Third Geological Exploration Institute, Henan Bureau of Geo-exploration and Mineral Development, Zhengzhou 450001, China³ Faculty of Science, University of Brunei Darussalam, Gadong BE1410, Brunei Darussalam⁴ Centre for Excellence in Ore Deposits (CODES), University of Tasmania, Hobart 7001, Australia

* Correspondence: any@ahu.edu.cn; Tel.: +86-0551-63861441

Received: 8 June 2019; Accepted: 26 July 2019; Published: 30 July 2019



Abstract: The occurrence of pyrite concretions in the Permian Longtan Formation sheds light on the paragenesis, formation conditions and regional paleoenvironment. We analyzed the mineral and geochemical characteristics of pyrite concretions using scanning electron microscopy-energy dispersive spectrometer (SEM-EDS), X-ray diffraction (XRD) and laser ablation inductively coupled plasma mass spectrometry (LA-ICP-MS) from the Longtan Formation shales in Anhui, Eastern China. These pyrite concretions consist of two types, each with a distinct nucleus and outer layer: The former is mainly made up of quartz, bivalve fragments and minor gypsum, ankerite, siderite and pyrite, the latter consists of pyrite (FeS₂) in the voids of quartz. Based on the correlation matrix and geochemical/mineralogical affinity, trace elements in the pyrite concretions fall into three groups, that is, I (Sr, Ba, Rb and K) in calcic minerals from bivalve-bearing nucleus, II (Nb, Ta, Zr and Hf) in certain heavy minerals and III (V, Cr, Co and Ni) in pyrites. Mineral assemblage and paragenetic analysis show that the formation of pyrite concretions can be divided into three stages: (1) deposition of bivalve-bearing nucleus, (2) lithification of diatoms and (3) diagenesis of pyrite. Mineral and geochemical indicators suggest that the formation environment of pyrite concretions has undergone a major shift from lagoon with intense evaporation, to strong reducing marsh.

Keywords: pyrite concretions; Longtan Formation; Permian; LA-ICP-MS mineral geochemistry; sedimentary pyrite; Anhui (Eastern China)

1. Introduction

Mineral concretions in sedimentary rocks, including ferromanganese (Fe-Mn), Co-rich, siderite and phosphorite ones, contain potential important (non)-metallic resources [1–6] and record many important diagenetic and paleoenvironmental information [5–8]. Although increasing studies tend to divide concretions into three main types, that is, syngenetic, diagenetic and epigenetic [9–11], all of them record the composition and conditions of the surrounding sediment layers [5,6]. Pyrite concretions record the sedimentary formation processes [7,8], the subsequent metasomatic growth and/or alteration [12,13], microbial sulphate reducing pyrite formation versus later-formed (metasomatic or hydrothermal related) pyrite formation [12,13] and thus determine the mineral and geochemical characteristics of pyrite concretions are highly important [8]. A large number of pyrite concretions were recently found from the Longtan Formation (Chaohu, Eastern China), whose genesis and sedimentary environment are still unclear [14,15]. In this paper, we tackle this issue from a mineralogical and geochemical perspective of pyrite concretions. Using scanning electron microscopy-energy dispersive spectrometer (SEM-EDS)

and laser ablation inductively coupled plasma mass spectrometry (LA-ICP-MS) analyses [16–18], we identified the composition of nucleus and rims of pyrite concretions and proposed that pyrite concretions were formed in multiple stages of diagenesis and metasomatism. This paper offers new insight into the sedimentary conditions of the Longtan Formation.

2. Geological Setting

The Upper Permian Longtan Formation is exposed in the Pingdingshan area (Chaohu city, Anhui Province) in Eastern China (Figure 1a,b). Geologically, the study area lies on the northwestern margin of the Yangtze Plate [19]. Local stratigraphy consists mainly of Silurian to Permian and Jurassic sequences (Figure 1c) The Permian sequences at Chaohu comprise (from bottom up) the Qixia, Gufeng, Longtan and Dalong Formations. The Permian sequences are overlain by the Lower Triassic Yinkeng Formation and overlie the Upper Carboniferous Chuanshan Formation [14,15]. The Longtan Formation is dominated by terrigenous clastic rocks, approximately 60 m thick and includes three members: The lower member consists of grayish-black siltstone, mudstone and shale with abundant fossils, such as brachiopods and gastropods. The middle member consists of (dark)-gray thick-bedded quartz sandstone with thin mudstone interbeds. The upper member consists of dark-grey mudstone with interbedded thin coal seams and thick bioclastic/micritic limestone. The pyrite concretions are exposed in the shale of the lower member (Figure 2), which was interpreted to have deposited in a swampy environment.

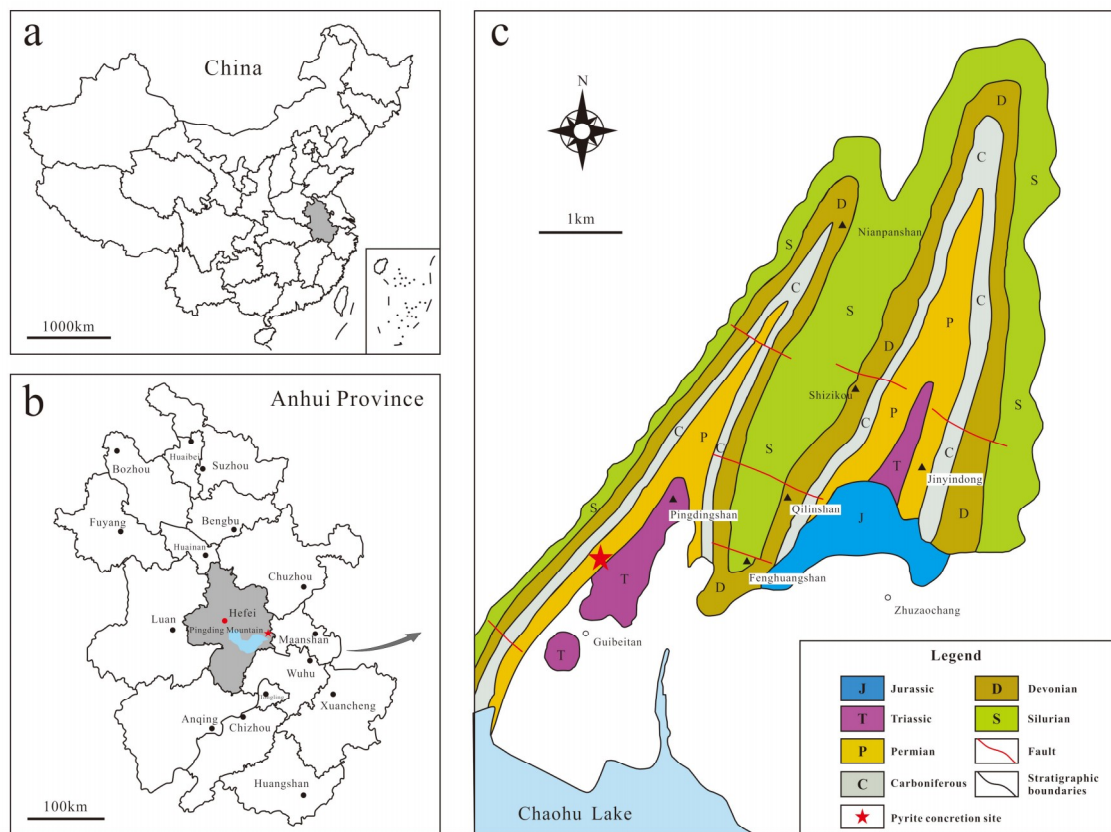


Figure 1. Map showing the location of concretions (a,b) and concretion-bearing sequences (c) in the Chaohu area (Anhui, Eastern China).

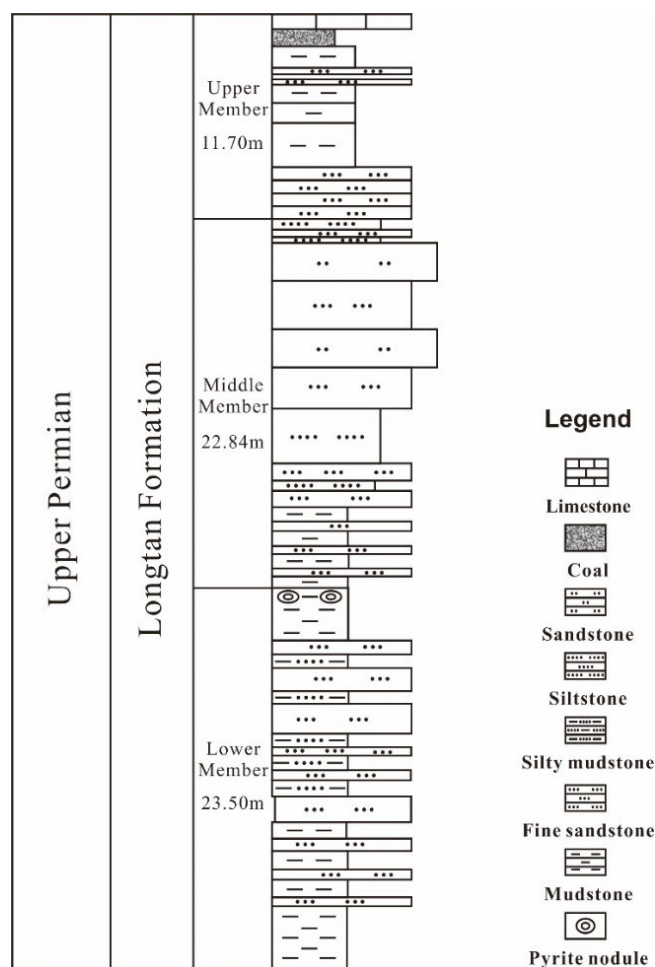


Figure 2. Stratigraphic column of the Upper Permian Longtan Formation at the Chaohu area, showing the locations of pyrite concretions.

3. Samples and Methods

Pyrite concretions ($n = 20$) were sampled from outcrops of the Longtan Formation in the Chaohu area and were processed at the Geological Laboratory of Anhui University. All concretions were analyzed using scanning electron microscopy (SEM) and X-ray diffraction (XRD) and the best-zoned concretion (based on SEM and XRD results) was processed with LA-ICP-MS spot analyses ($n = 18$). Analysis sites were chosen on the equatorial plane of concretions parallel to the bedding. Thin sections (about 60 μm thick) were observed with scanning electron microscopy (SEM, FE- Σ IGMA VP300, Carl Zeiss AG., Heidenheim, Germany) for the morphology and distribution of pyrite concretions at the Guangdong Provincial Key Laboratory of Mineral Resources and Geological Processes, Sun Yat-sen University. The samples were gold-coated with a Quorum Q150T ES sputtering coater. The working distance of the SEM-EDS was 10–16 mm using 10.0 kV beam voltage and 6 nm aperture with a 5 nm spot size. The images were captured via a retractable solid-state backscattered electron (BSE) detector. Mineral compositions of the powdered pyrite samples (200 mesh) were measured with a Rigaku SmartLab X-ray powder diffractometer (XRD, SmartLab 9kW, Rigaku Corporation, Tokyo, Japan) at the Modern Experimental Technology Center, Anhui University. The X-ray generator comprises a 9 kW rotating anode, which was operated at 40 kV, 100 mA and equipped with a single-crystal graphite monochromator. Power samples were scanned in the 2θ range of 5–90° with step size of 0.01°.

Elemental concentrations were measured with LA-ICP-MS (laser ablation inductively coupled plasma mass spectrometry) at the Laboratory of Sample Solution in Wuhan, China. The analysis was performed with a Resonetic RESOLution M-50 ArF-Excimer laser ablation system (Coherent Inc., Santa

Clara, CA, USA) coupled to an Agilent 7700 ICP-MS (Agilent Technologies, Santa Clara, CA, USA). Operating conditions include 193 nm wavelength and 80 mJ laser energy, 10 Hz frequency, 44 μm spot size and used He as the carrier gas. Element contents were calculated with the software ICPMS DataCal (Version 10.2, China University of Geosciences, Wuhan, China), an in-house program developed by the China University of Geosciences. The detection limits of trace elements were 2–8 ppb and the analytical precision was better than 5%, while the detection limits of major elements were greater than 0.1 wt. %.

4. Results

4.1. Texture of Pyrite Concretions

Most pyrite concretions are well-preserved in the black shale of the Lower Longtan Formation. The shales are laminated (2–5 mm thick) and comprise predominantly clay minerals. Lenticular coal seam ($0.2 \times 0.5 \text{ m} \sim 0.5 \times 2.5 \text{ m}$) and abundant sulfur occur in the shales (Figure 3a). Concretions cut through the bedding plane of surrounding rocks and no deformation was found along their contact. Equatorial planes of concretions are parallel to the bedding (Figure 3b). The concretions are mostly spheroidal and minor ellipsoidal or irregularly-shape. They are 4–15 cm in diameter with lateral spacing of about 5–10 cm. These concretions preserve the original depositional stratification of their hosting shales. The weathered surfaces are rough and are grayish yellow due to oxidation (Figure 3c). The concretions contain circumferential and radial structures in their cross section and their fresh surfaces can be divided into the dark-gray euhedral pyrite outer layer and the black nucleus organic matter (Figure 3d). Both the nucleus and outer layer are relatively dense and contain radial fractures between the former two. The central part of fractures is not filled (void) and there are abundant minerals along the void margin. The nucleus occupies one-third of the concretions.

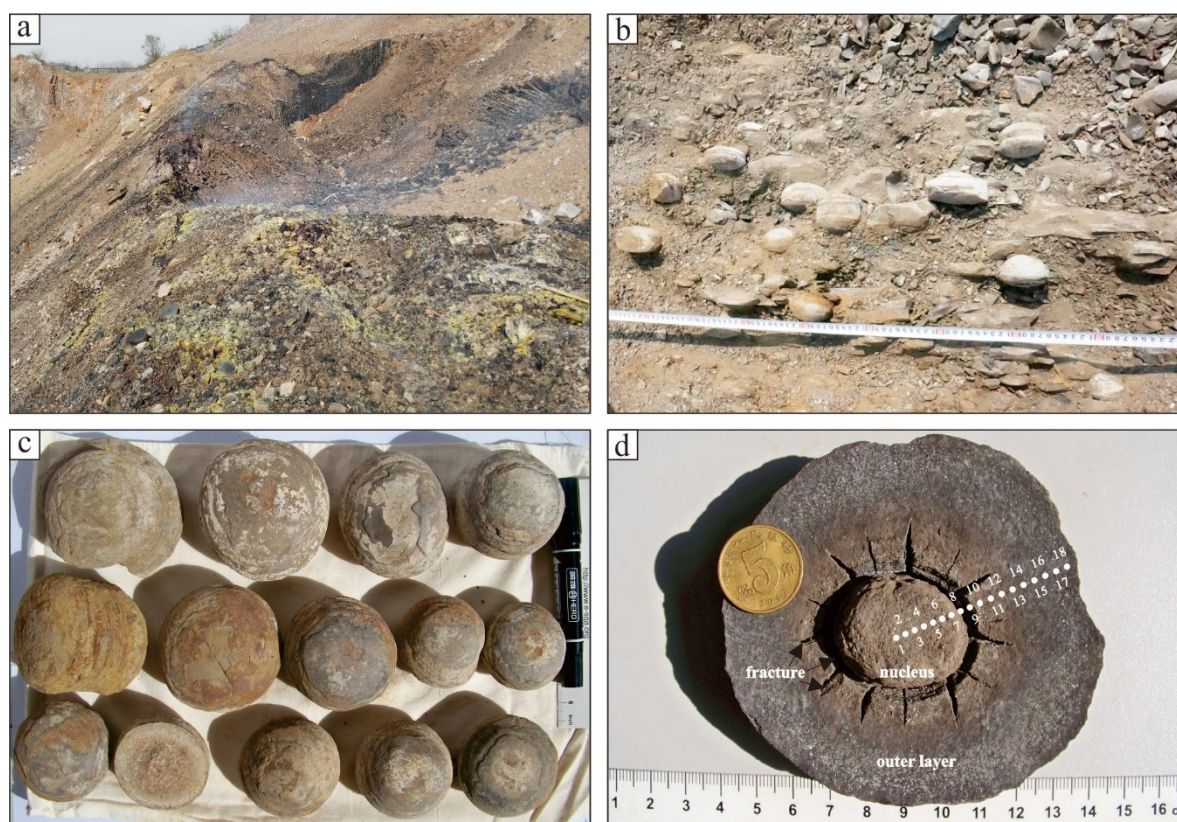


Figure 3. Photographs of pyrite concretions from the Longtan Formation at Pingdingshan. (a) Coal and abundant sulfur (smoke emitted from spontaneous combustion) occur in the shales; (b) Outcrops of pyrite concretions in the shales; (c) Individual pyrite concretions; (d) Cross-section of a pyrite concretion, showing the nucleus and the outer layer. White dots denote the LA-ICP-MS analysis spots.

4.2. SEM Imaging

SEM-backscattered electron (BSE) imaging of different parts of the concretion nucleus and outer layer were conducted. The nucleus mainly consists of bivalve fossils and surrounded layers (Figure 4a). While the former shows features such as symmetric shells, concentric patterns and curved beaks (566 to 877 μm in shell width; Figure 4b), the latter represents a diatom layer with abundant porous (Figure 4c). Aggregated, acicular and platy crystals are visible in the cavities of the bivalves (Figure 4d). The main constituent of the outer layer is fine-medium pyrite crystals, which are in the forms of cube $a\{100\}$, octahedron $o\{111\}$ and pentagonal dodecahedron $e\{210\}$ (Figure 4e). Pyrite crystals are angular polyhedral and those closer to the outer layer margin are coarser and better crystallized. Fine-grained pyrite crystals are visible near the nucleus. Striations on adjacent planes of the porous pyrite crystals are perpendicular to each other and the fractures between them are distinct under high magnification ($\times 1500$) (Figure 4f).

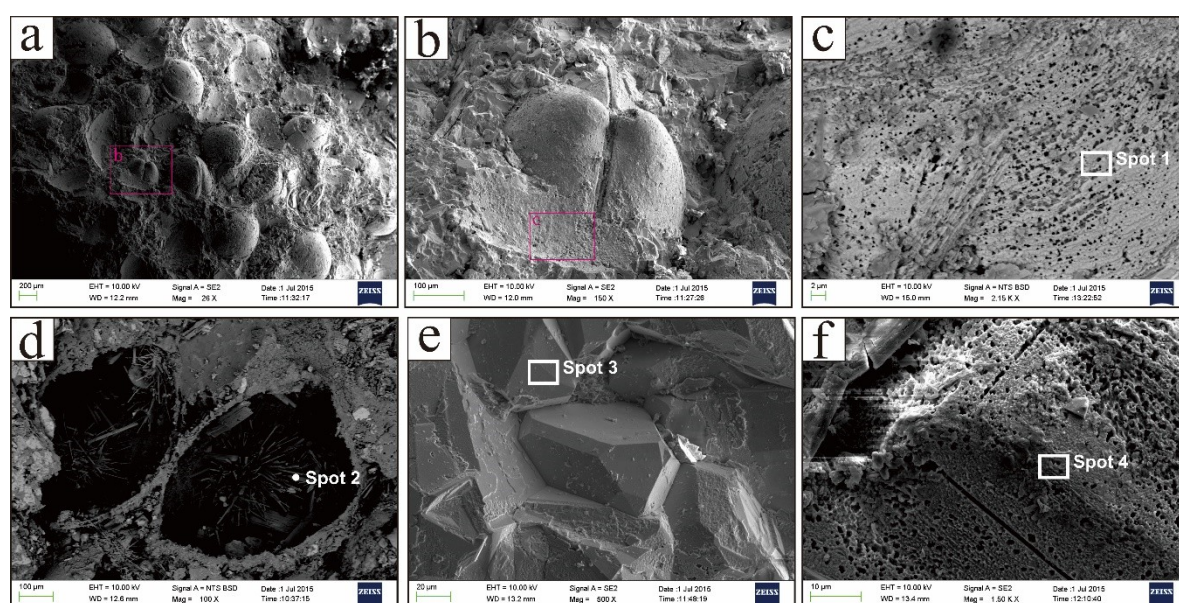


Figure 4. Microstructure of pyrite concretions under scanning electron microscope (SEM). (a) Abundant bivalve fossils in the nucleus; (b) A bivalve with curved beak; (c) Porous layer in the nucleus; (d) Acicular and platy crystals in the bivalve cavities; (e) Different forms of individual pyrite crystals in out layer; (f) Porous crystalline pyrite crystals. Note: Spot 1–4 are the scanning electron microscopy-energy dispersive spectrometer (SEM-EDS) spots and (b) and (c) are the zoom-in of the pink-line boxes in (a) and (b), respectively.

In addition, four energy dispersive spectrometric (EDS) points of diatom layer in the nucleus (Spot 1), acicular and platy crystals in the bivalve cavities (Spot 2) and individual pyrite crystals (Spot 3) and porous pyrite (Spot 4) in the outer layer were analyzed in this study. The EDS spectrum of Spot 1 are composed of oxygen (61.05 atom %) and silicon (36.02 atom %) (Figure 5a), indicating that the mineral of porous diatom layer around the bivalve is most probably quartz (SiO_2). Results of Spot 2 is composed of oxygen (40.91 atom %), sulfur (27.51 atom %) and calcium (30.63 atom %) show that the acicular and platy crystals in the bivalve are gypsum (CaSO_4) (Figure 5b). Meanwhile, the EDS results of Spot 3 confirm that individual pyrite in the outer layer comprises predominantly pyrite (FeS_2) (Figure 5c), whilst those of spot 4 of porous pyrite (contains sulfur, iron and minor silicon and oxygen) suggest the presence of diatom remnants/pseudomorphs (Figure 5d).

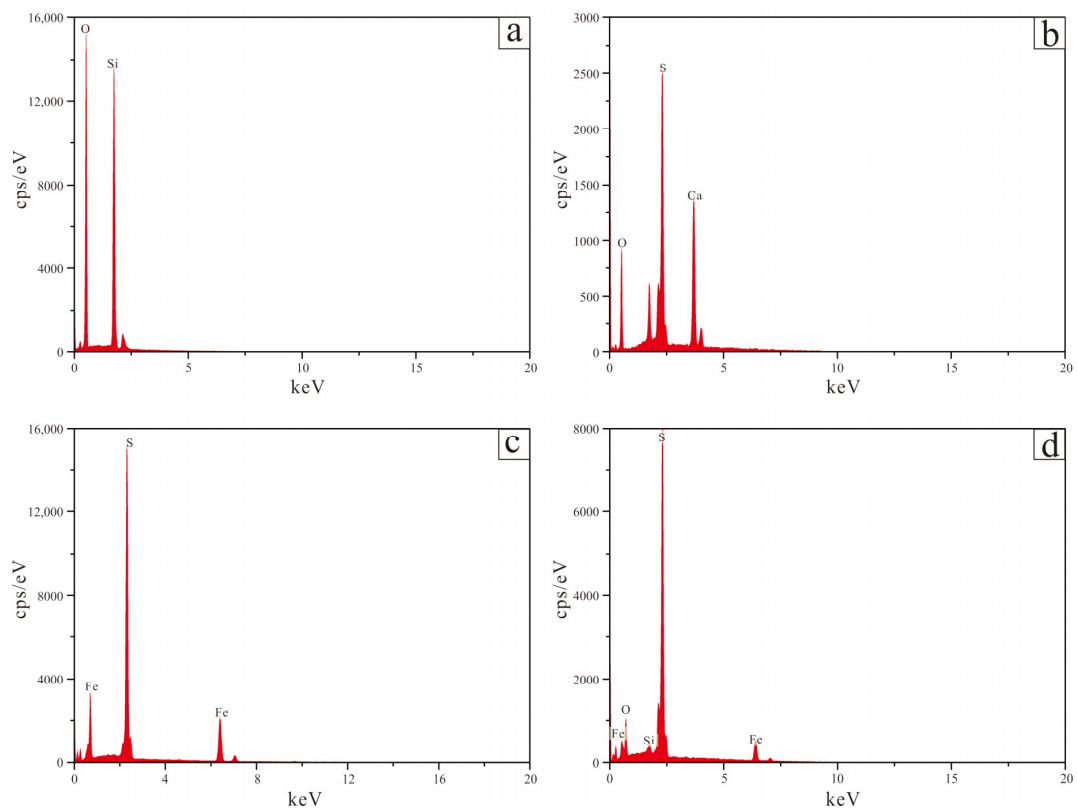


Figure 5. SEM-EDS spectra of different minerals in pyrite concretions. (a) Diatom layer in the nucleus (Spot 1); (b) acicular and platy crystals in the bivalve (Spot 2); (c) pyrite crystals in the outer layer (Spot 3); (d) porous pyrite in the outer layer (Spot 4).

4.3. XRD

XRD patterns of the pyrite concretions are shown in Figure 6. The results show that the main mineral of the concretions is quartz and pyrite. The nucleus comprises mainly quartz, pyrite with minor gypsum, ankerite and siderite (Figure 6a), whilst the outer layer comprises predominately pyrite with trace quartz (Figure 6b). The proportion and degree of crystallization of pyrite in the outer layer is markedly higher than that in the nucleus.

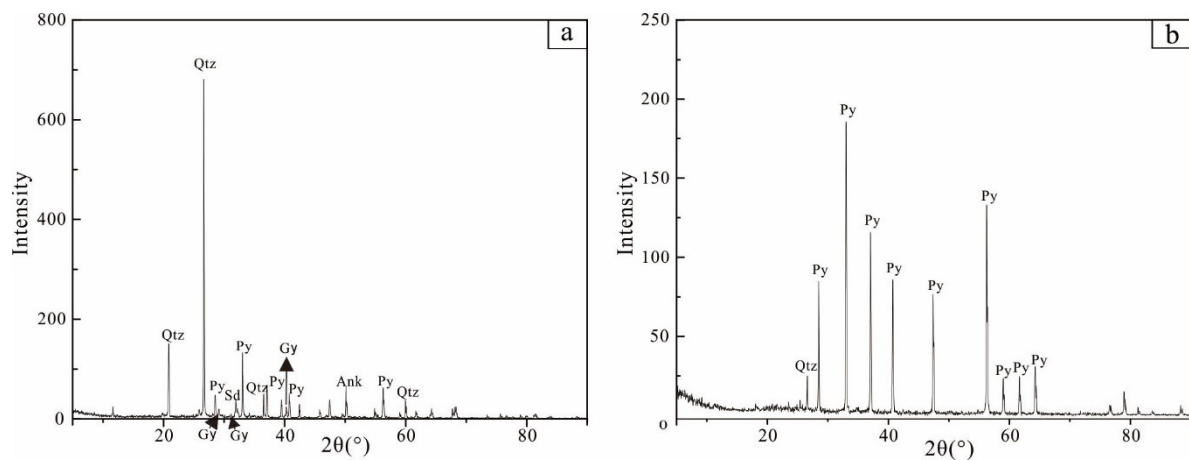


Figure 6. X-ray diffraction (XRD) patterns for the pyrite concretions from Pingdingshan: (a) Nucleus; (b) Outer layer. Abbreviations: Qtz, Quartz; Py, Pyrite; Gy, gypsum; Ank, Ankerite; Sd, Siderite.

4.4. LA-ICP-MS Mineral Geochemistry

The LA-ICP-MS geochemical results of the pyrite concretions are shown in Table 1. All main elements (>0.1 wt. %) are shown as oxides except iron and sulfur in the form of pyrite (FeS_2). Based on the 2:1 ratio between water (H_2O) and quartz (SiO_2), it is considered that the water (H_2O) should be crystalline water in quartz (SiO_2) and record as $\text{SiO}_2 \cdot 2\text{H}_2\text{O}$. Trace elements are expressed in ppm.

Except for Spots 8 and 9 in the fissure between the nucleus and outer layer (Figure 3d), the FeS_2 and $\text{SiO}_2 \cdot 2\text{H}_2\text{O}$ contents account for 91.79–99.41 wt. %. The nucleus contains mainly $\text{SiO}_2 \cdot 2\text{H}_2\text{O}$ (66.37–91.14 wt. %), FeS_2 (1.89–25.81 wt. %) and Al_2O_3 (2.07–3.66 wt. %) and minor K_2O (0.43–1.07 wt. %), CaO (0.46–1.78 wt. %) and P_2O_5 (0.38–1.03 wt. %), while the outer layer contains mainly FeS_2 (57.38–98.12 wt. %) and with a very wide range $\text{SiO}_2 \cdot 2\text{H}_2\text{O}$ (1.29–39.15 wt. %) and low Al_2O_3 (0.23–1.89 wt. %). Major element contents in the nucleus are significantly higher than those of the outer layer, whereas the FeS_2 content of the nucleus is lower (Table 1).

In addition, trace elements in the nucleus and outer layer mainly fall into three groups based on the correlation matrix or geochemical (Figure 7) and mineralogical affinity [20]. The 1st group (Sr, Ba, K and Rb) is correlated with CaO and P_2O_5 in the nucleus and is mostly associated with the bivalve nucleus [21]. The 2nd group (Nb, Ta, Zr and Hf) is related to diatomite ($\text{SiO}_2 \cdot 2\text{H}_2\text{O}$) across the whole concretion. We speculate that the 2nd group elements may have occurred in diatomite [22]. Meanwhile, the 3rd group (Co, Ni, V and Cr) is associated with pyrite (FeS_2) centralized in the entire concretion and their contents gradually increase from inside out [23].

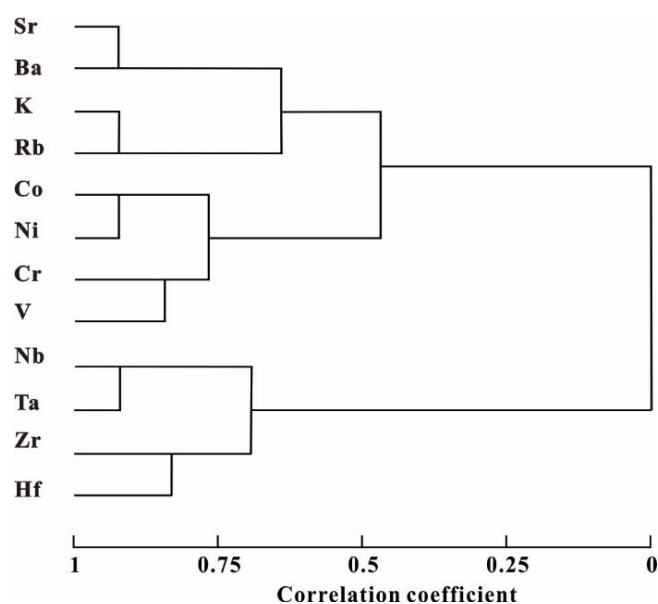


Figure 7. Clustering analysis diagrams of trace elements in the pyrite concretions from the Chaohu area.

Table 1. Laser ablation inductively coupled plasma mass spectrometry (LA-ICP-MS) geochemical results (ppm) of the pyrite concretions from Pingdingshan.

Number	1	2	3	4	5	6	7	8	9	10	11	12	13	14	15	16	17	18
Position	Nucleus									Outer Layer								
FeS ₂	1.89	5.85	5.52	8.72	10.25	11.41	25.81	25.71	12.18	57.38	65.33	79.64	82.61	87.72	92.58	91.87	97.01	98.12
SiO ₂ ·2H ₂ O	91.14	86.51	86.69	83.07	82.45	81.91	66.37	65.17	61.43	39.15	30.04	17.37	13.64	8.01	4.50	5.59	2.28	1.29
Al ₂ O ₃	3.37	3.66	2.90	2.07	3.59	3.17	3.54	2.17	4.20	0.79	1.45	1.89	1.25	1.36	0.87	1.00	0.38	0.23
K ₂ O	0.54	0.47	0.43	1.07	0.56	0.58	0.49	0.39	0.68	0.14	0.26	0.02	0.23	0.63	0.18	0.18	0.01	0.01
CaO	0.59	0.67	1.37	1.78	0.46	0.62	0.79	2.87	11.66	0.66	1.14	0.05	0.74	0.48	0.72	0.24	0.04	0.05
P ₂ O ₅	0.49	0.43	0.97	1.03	0.38	0.47	0.41	0.99	2.02	0.20	0.42	0.07	0.33	0.54	0.39	0.40	0.04	0.01
K ₂ O	0.54	0.47	0.43	1.07	0.56	0.58	0.68	0.49	0.39	0.14	0.26	0.02	0.23	0.63	0.18	0.18	0.01	0.01
SrO	0.20	0.12	0.50	0.05	0.08	0.09	0.14	1.30	3.20	0.04	0.06	0.00	0.07	0.02	0.09	0.04	0.00	0.00
BaO	0.05	0.03	0.12	0.01	0.03	0.03	0.04	0.24	0.59	0.01	0.01	0.00	0.02	0.01	0.02	0.01	0.00	0.00
total	98.82	98.22	98.92	98.88	98.36	98.84	98.27	99.31	96.35	98.52	98.97	99.05	99.12	99.38	99.54	99.52	99.79	99.73
K	4514	3935	3551	8917	4624	4772	5635	4066	3219	1149	2138	134	1949	5190	1506	1527	114	111
Sr	1665	1004	4208	383	717	782	1159	11032	27051	378	520	3.62	593	176	768	319	8.11	5.81
Ba	486	258	1107	106	232	248	338	2116	5275	94.6	133	5.51	158	53.9	214	77.1	4.11	3.66
Rb	25.86	23.53	19.86	53.7	26.5	27.6	24.0	18.4	32.06	6.46	13.1	0.47	13.1	40.6	8.92	10.6	0.70	0.74
V	142	107	287	68.7	101	91.4	112	227	507	42.4	82.3	42.7	73.0	57.1	88.8	120	15.6	6.07
Co	0.69	1.53	1.67	4.77	2.31	2.04	3.27	4.65	20.3	5.44	6.40	0.29	5.76	5.11	7.56	3.83	0.21	0.67
Ni	4.27	8.70	11.6	21.2	13.2	13.5	19.5	33.2	70.2	29.8	34.4	4.70	29.1	19.3	28.2	16.6	3.34	3.21
As	3.50	7.69	9.98	3.49	8.67	9.51	9.81	14.2	16.4	12.4	10.2	6.69	10.6	28.9	16.5	25.5	6.05	9.20
Nb	2.26	3.43	1.89	1.67	2.23	2.41	3.06	3.98	2.70	0.82	2.20	0.01	3.19	1.35	2.20	1.52	0.18	0.27
Ta	0.20	0.26	0.14	0.13	0.16	0.21	0.20	0.29	0.18	0.06	0.22	0.00	0.35	0.13	0.24	0.13	0.02	0.02
Zr	84.6	75.5	89.2	71.1	84.2	86.4	76.2	62.2	100	28.2	45.0	5.23	43.1	73.7	53.4	22.1	2.71	1.44
Hf	1.07	1.07	1.07	0.87	1.09	1.27	1.09	0.85	1.41	0.50	0.84	0.11	0.79	1.85	1.16	0.47	0.10	0.04

5. Discussion

5.1. Formation Stage of Pyrite Concretions

Pyrite concretions in sedimentary rocks, including deposited, lithificated and diagenetic type, are formed by the aggregation of authigenic minerals [9,12]. These minerals usually consist of several kinds and formed in different stages [24,25]. For this reason, paragenetic association of minerals in pyrite concretions can be used to reveal the formation of concretion [7,26]. According to the SEM-EDS and XRD results, the mineral compositions of the nucleus and outer layer are clearly different from each other: the former is mainly made up of quartz, with minor gypsum, pyrite, ankerite and siderite, whereas the latter consists mainly of pyrite and quartz.

Gypsum, ankerite and siderite crystals in the nucleus are mainly preserved in the bivalve fossils and the quartz occurs mainly as porous diatomite filling with some pyrite grains in the bivalves. Based on the distributions of minerals and bivalves in the nucleus, it is inferred that the gypsum was likely be formed before the bivalve fossils [10] and minerals around the bivalve (e.g., pyrite, quartz) may have formed after the burial of the bivalves [9]. In the outer layer, pyrites occurs mainly as fine-grained pyrite filled in diatomite pore or cubic pyrite with minor diatom residue on the crystal surface. This indicates that the pyrite was formed after the porous diatomite [1].

Meanwhile, the relationship between pyrite (FeS_2) and diatomite ($\text{SiO}_2 \cdot 2\text{H}_2\text{O}$) has also been clarified from all the concretions. FeS_2 and $\text{SiO}_2 \cdot 2\text{H}_2\text{O}$ show negative correlations (Figure 8a) and the percentage of $\text{SiO}_2 \cdot 2\text{H}_2\text{O}$ decline and FeS_2 ratio accordingly increase from the nucleus to the outer layer (Figure 8b). The components of FeS_2 and $\text{SiO}_2 \cdot 2\text{H}_2\text{O}$ in the concretions indicate that the diatomite is mainly enriched in the nucleus, while the pyrite is primarily concentrated in the outer layer. Distribution characteristics of the diatomite may be related to the growth habits of diatoms, which gradually become looser from the nucleus to outer layer [27]. Pyrite enrichment in the outer layer is probably the result of pyrite filling in the voids of diatom, which becomes gradually denser from the nucleus to the outer layer [1].

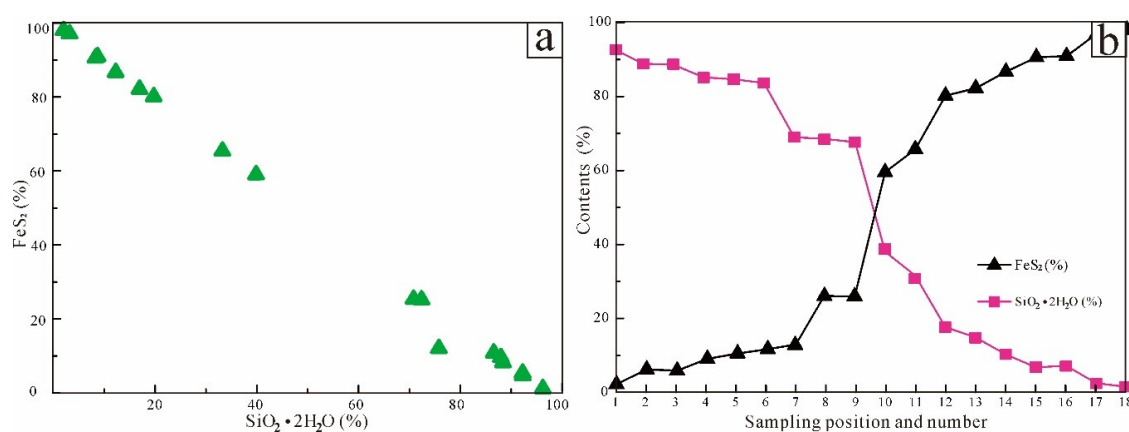


Figure 8. Diagrams of pyrite (FeS_2) and diatomite ($\text{SiO}_2 \cdot 2\text{H}_2\text{O}$) contents in the pyrite concretions from the Pingdingshan area. (a) Pyrite (FeS_2) versus diatomite ($\text{SiO}_2 \cdot 2\text{H}_2\text{O}$) contents in the pyrite concretions; (b) The contents of pyrite (FeS_2) and diatomite ($\text{SiO}_2 \cdot 2\text{H}_2\text{O}$) in the pyrite concretions.

According to the paragenetic relations of minerals and other components, the formation of pyrite concretions can be divided into three main stages: (1) deposition of bivalve-bearing nucleus and gypsum; (2) lithification of diatomite around the bivalve-bearing nucleus; (3) diagenesis of pyrite in the voids of diatomite.

5.2. Formation Environment of Pyrite Concretions

Different parts of the pyrite concretions in the Longtan Formation were likely formed in different sedimentary environments and recorded the corresponding environmental information [28,29].

The presence of gypsum in the bivalve fossils indicates that the nucleus has likely come from an arid and oxidizing environment [30–32]. The main composition of the concretions around the nucleus is diatomite ($\text{SiO}_2 \cdot 2\text{H}_2\text{O}$) with no detrital particles and carbonate rocks. This supports that these diatoms were formed in shallow water translucent zone [9] but suggests that the seawater in that environment contains few clastic materials [33,34]. These barren seas was so nutritionally deficient for diatoms that they have to grow around the nucleus to get nutrients [35,36]. Differently, diagenetic pyrite filled in the voids of diatomite represents restore environment. It is speculated that the environment of pyrite diagenesis may be marsh facies in Longtan Formation [9].

Salinity of water and sedimentary facies can be determined by the 1st group elements and their ratios (e.g., Sr/Ba ratio and the Rb/K ratio) in sedimentary rocks. The Sr/Ba and Rb/K ratios of river and fresh-water lake are generally lower than those of marine sediments [37,38]. Sr/Ba ratios of the bivalve nucleus are of 1.59 to 5.21 (all >1), which may suggest salty-water and marine deposits [38,39]. The Rb/K ratio of bivalve nucleus (0.0056–0.006) is above 0.004 but below 0.006, which indicate sea-land transitional facies [37]. Therefore, it is inferred that the nucleus of concretion of this study should be formed in the evaporative microfacies of marine environments near the sea-land transitional facies, possibly lagoonal, environment.

The 2nd group elements (Nb, Ta, Zr and Hf) occur commonly in certain heavy minerals (e.g., columbites, zircon) and can infer the element source and formation environment [40]. The concentrations of Nb and Ta, Zr and Hf are positively correlated with each other in this study (Figure 9), showing that the nucleus and outer layer should not have similar provenance. A marked difference of ratio and contents of Zr and Hf, Nb and Ta between the nucleus and the outer layer infer that the diatom in the nucleus and pyrite in the outer layer were probably formed in different environments [41]. The narrower deviation in the nucleus than the outer layer suggests that the formation environment of bivalve-hosting diatom nucleus is calmer than the outer pyrite layer [42].

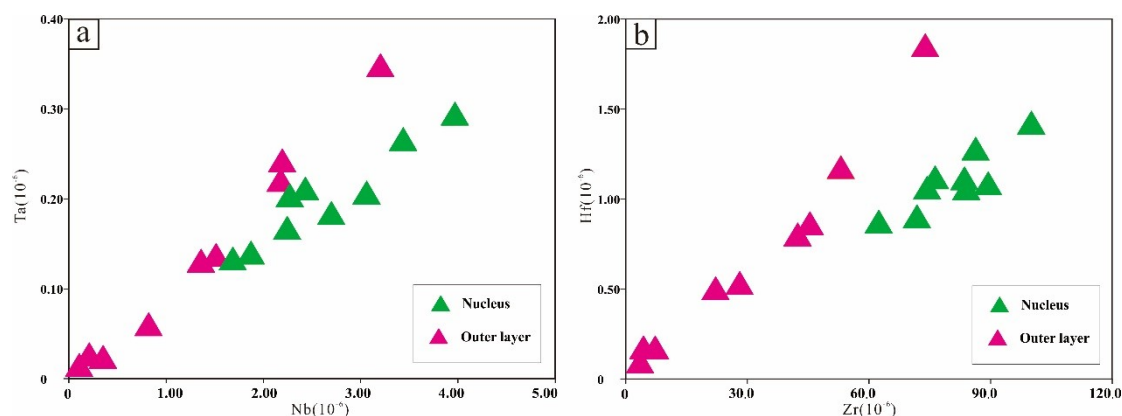


Figure 9. Binary diagrams of Ta, Nb, Hf, Zr contents in the nucleus and outer layer of pyrite concretions from the Chaohu area. (a) Ta versus Nb; (b) Hf and Zr.

Elements of the 3rd group (V, Cr, Co and Ni) could replace Fe^{2+} of pyrites and the Co/Ni ratio can indicate the genetic types of pyrites [43]. The Co/Ni ratios in these pyrite concretions are of 0.06 to 0.27 (<1), representing a sedimentary origin [43]. The strong linear Co versus Ni relationship suggests that these pyrite grains were deposited in a similar time. Compared to Ni, V is more easily accumulated in anoxic condition or in organic-rich sediments. Therefore, the high V/(V + Ni) ratios represent a strong hypoxic environment. V/(V + Ni) ratios of the pyrite concretions are of 0.59 to 0.97, showing predominantly hypoxic and sulfidic environments based on the classification of Zhang et al. (2011) [44].

Combined with mineralogical evidence, we suggest that the formation environment of pyrite in the voids of diatomite was likely a hypoxic and sulfidic marshy environment.

5.3. Three-Stage Formation Model of Pyrite Concretions

Depositional formation of the gypsum-bearing bivalve: the paleoenvironment of the lower Yangtze region in the Chaohu area was possibly a sea-land transitional lagoonal environment [33]. In the lagoon, there are large bivalves with gypsum precipitated on them during evaporation events [45]. These bivalves were swept into the sea by waves and turned into the bivalve nucleus via abrasion (Figure 10a).

Lithification formation of diatomite concretion: Some diatoms are nourished by organic-rich bivalve in the sea [22]. They grew and aggregated around the bivalve nucleus, forming diatom nodules [46]. Presumably, the bivalves are the actual physical nucleation points. In these diatom nodules, the earlier diatoms are generally denser in the interior and the later-formed diatoms in the outer layer are looser than the interior (Figure 10b).

Diagenetic formation of pyrite: Sedimentary environment in the study area quickly turned into a marshy environment. The diatom nodules were buried rapidly by fine carbonaceous detrital sediments [12]. During the diagenesis, this biodetritus may have released sulfur-bearing and strongly reducing fluids [9,47]. They combined with ferrous ions to form pyrite and fill the voids of diatoms [48]. The pyrites formed in the outer layer prevented seawater from entering into the concretion interior, resulting in lesser amount of pyrite in the nucleus (Figure 10c).

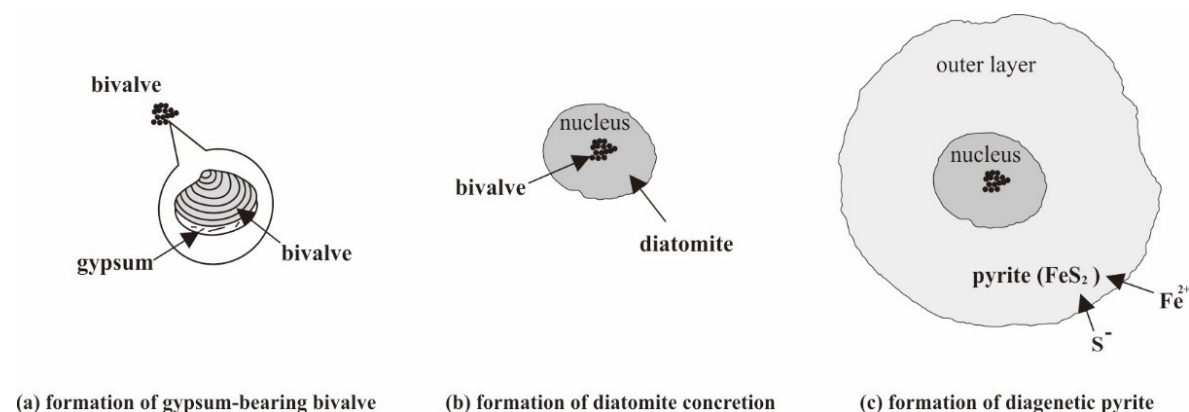


Figure 10. Sketch map of formation model of pyrite concretions from Chaohu. (a) Depositional formation of gypsum-bearing bivalve, (b) Lithification formation of diatomite concretion, (c) Diagenetic formation of pyrite concretion.

6. Conclusions

(1) Compositions between the nucleus and outer layer of pyrite concretions are clearly different from each other. The former is mainly made up of quartz, bivalve fragments and minor gypsum, ankerite, siderite and pyrite, whilst the latter consists of pyrite in the voids of quartz.

(2) Mineral paragenesis indicates that the formation of pyrite concretions has undergone three stages: (1) deposition of gypsum-bearing bivalve, (2) lithification of diatomite concretion, (3) diagenesis of pyrite concretion.

(3) We speculate that the formation environment of pyrite concretions has undergone a major shift from sedimentary to diagenetic stage. The early sedimentary environment was likely a nutrient-poor sea-land transitional lagoon with intense evaporation, while the diagenetic environment was likely strongly reductive marshy environment with abundant clastic/carbonaceous detritus supply.

Author Contributions: Conceptualization, Y.A.; methodology, Q.H. and Y.A.; validation, Q.H. and F.S.; investigation, Y.A.; resources, F.S.; data curation, Y.A. and Q.H.; writing—original draft preparation, Q.H.; writing—review and editing, Y.A. and C.L.; supervision, C.L.; funding acquisition, Y.A. and Q.H.

Funding: This work was funded by the National Natural Science Foundation of China (41802006, 41602173), the Natural Science Foundation of Anhui Province (1708085QD86) and the University Natural Science Research Project of Anhui Province (KJ2018A0005).

Acknowledgments: We thank Yixiang Chen, Sen Yang, Qin Jiang, Qianwen Sun, Yu Wang, Qikuan Zhu and Yuangao Sun (Anhui University) for their sampling support.

Conflicts of Interest: The authors declare no conflict of interest.

References

1. Steadman, J.A.; Large, R.R.; Meffre, S.; Olin, P.H.; Danyushevsky, L.V.; Gregory, D.D.; Belousov, I.; Lounejeva, E.; Ireland, T.R.; Holden, P. Synsedimentary to early diagenetic gold in black shale-hosted pyrite nodules at the Golden Mile Deposit, Kalgoorlie, Western Australia. *Econ. Geol.* **2015**, *110*, 1157–1191. [[CrossRef](#)]
2. Tarawneh, K.; Moumani, K. Petrography, chemistry and genesis of phosphorite concretions in the Eocene Umm Rijam Chert limestone Formation, Ma'an area, South Jordan. *J. Asian Earth Sci.* **2006**, *26*, 627–635. [[CrossRef](#)]
3. Hein, J.R.; Conrad, T.; Dunham, R.E. Seamount characteristics and mine-site model applied to exploration- and mining-lease-block selection for cobalt-rich ferromanganese crusts. *Mar. Georesour. Geotechnol.* **2009**, *27*, 160–176. [[CrossRef](#)]
4. Zhamoida, V.; Grigoriev, A.; Ryabchuk, D.; Evdokimenko, A.; Kotilainen, A.; Vallius, H.; Kaskela, A.M. Ferromanganese concretions of the eastern Gulf of Finland—Environmental role and effects of submarine mining. *J. Mar. Syst.* **2017**, *172*, 178–187. [[CrossRef](#)]
5. Benites, M.; Millo, C.; Hein, J.; Nath, B.N.; Murton, B.; Galante, D.; Jovane, L. Integrated geochemical and morphological data provide insights into the genesis of ferromanganese nodules. *Minerals* **2018**, *8*, 488. [[CrossRef](#)]
6. Hendry, J.P.; Pearson, M.J.; Trewin, N.H.; Fallick, A.E. Jurassic septarian concretions from NW Scotland record interdependent bacterial, physical and chemical processes of marine mudrock diagenesis. *Sedimentology* **2006**, *53*, 537–565. [[CrossRef](#)]
7. Lopez, L.; Lo Monaco, S.; Escobar, G.; Camargo, C.; Lugo, P.; Rojas, H.; Gonzalez, C. Study of pyrite nodules from Querecual Formation, Anzoategui state (Venezuela) by with electron probe microanalysis. *Acta Microsc.* **2009**, *18*, 333–343.
8. Johanna, M.C.; Claire, R.B.; Andrey, B. Coupled Fe and S isotope variations in pyrite nodules from Archean shale. *Earth Planet. Sci. Lett.* **2014**, *392*, 67–79.
9. Xiao, S.; Schiffbauer, J.D.; McFadden, K.A.; Hunter, J. Petrographic and SIMS pyrite sulfur isotope analyses of Ediacaran chert nodules: Implications for microbial processes in pyrite rim formation, silicification, and exceptional fossil preservation. *Earth Planet. Sci. Lett.* **2010**, *297*, 481–495. [[CrossRef](#)]
10. Wang, X.; Zhang, S.; Wang, H.; Canfield, D.E.; Su, J.; Hammarlund, E.U.; Bian, L.Z. Remarkable preservation of microfossils and biofilms in Mesoproterozoic silicified bitumen concretions from Northern China. *Geofluids* **2017**. [[CrossRef](#)]
11. Nemra, A.; Mehadji, A.O.; Munnecke, A.; Belkhedim, S.; Belkebir, L. Carbonate concretions in Miocene mudrocks in NW Algeria: Types, geochemistry, and origins. *Facies* **2019**, *65*, 17. [[CrossRef](#)]
12. Goldberg, T.; Mazumdar, A.; Strauss, H.; Shields, G. Insights from stable S and O isotopes into biogeochemical processes and genesis of Lower Cambrian barite-pyrite concretions of South China. *Org. Geochem.* **2006**, *37*, 1278–1288. [[CrossRef](#)]
13. Cotroneo, S.; Schiffbauer, J.D.; McCoy, V.; Wortmann, U.G.; Darroch, S.A.F.; Peng, Y.; Laflamme, M. A new model of the formation of Pennsylvanian iron carbonate concretions hosting exceptional soft-bodied fossils in Mazon Creek, Illinois. *Geobiology* **2016**, *4*, 543–555. [[CrossRef](#)] [[PubMed](#)]
14. Zhu, Z.; Jiang, S.; Liu, G.; Zhao, K. Precise dating of the Middle Permian: Zircon U-Pb geochronology from volcanic ash beds in the basal Gufeng Formation, Yangtze region, South China. *Gondwana Res.* **2013**, *23*, 1599–1606. [[CrossRef](#)]

15. Jin, X.; Li, Z.; Feng, L.; Ma, X.; Zhou, Y. Study on sedimentary environment and coal accumulation characteristics of Longtan Formation in Chaohu Area. *Coal Sci. Technol.* **2014**, *42*, 92–96, (In Chinese with English Abstract).
16. An, Y.; Chen, Y.; Zhang, S.; Li, X.; Lai, C. New Discovery of Post-Magmatic Pyrite in Natural Coke at Yangliu Coalmine, Northern China. *Acta Geol. Sin.* **2018**, *6*, 2436–2437.
17. Gourcerol, B.; Kontak, D.J.; Thurston, P.C.; Petrus, J.A. Results of LA-ICP-MS sulfide mapping from Algoma-type BIF gold systems with implications for the nature of mineralizing fluids, metal sources, and deposit models. *Miner. Depos.* **2018**, *53*, 871–894. [[CrossRef](#)]
18. An, Y.; Liu, L.; Wang, M.; Zheng, S.; Guo, Y.; Zhang, S.; Lai, C. Source and Enrichment of Toxic Elements in Coal Seams around Mafic Intrusions: Constraints from Pyrites in the Yuandian Coal Mine in Anhui, Eastern China. *Minerals* **2018**, *8*, 164. [[CrossRef](#)]
19. Lin, C.; Zhang, X.; Yu, J.; Li, D.; Zhang, N. Sedimentary and Geochemical Characteristics of the Early Triassic Yinkeng Formation at West Pingdingshan Section in Chaohu, Anhui Province. *Acta Geol. Sin.* **2015**, *89*, 2363–2373, (In Chinese with English Abstract).
20. Hlawatsch, S.; Neumann, T.; Van den Berg, C.M.G.; Kersten, M.; Harff, J.; Suess, E. Fast-growing, shallow-water ferro-manganese nodules from the western Baltic Sea: Origin and modes of trace element incorporation. *Mar. Geol.* **2002**, *182*, 373–387. [[CrossRef](#)]
21. Mozley, P.S.; Davis, J.M. Internal structure and mode of growth of elongate calcite concretions: Evidence for small-scale, microbially induced, chemical heterogeneity in groundwater. *Geol. Soc. Am. Bull.* **2005**, *117*, 1400–1412. [[CrossRef](#)]
22. Kadko, D.; Burckle, L. Manganese nodules growth rates determined by fossil diatom dating. *Nature* **1980**, *287*, 725–726. [[CrossRef](#)]
23. Raiswell, R.; Bottrell, S.H.; Dean, S.P.; Marshall, J.D.; Carr, A.; Hatfield, D. Isotopic constraints on growth conditions of multiphase calcite–pyrite–barite concretions in Carboniferous mudstones. *Sedimentology* **2002**, *49*, 237–254. [[CrossRef](#)]
24. Raiswell, R.; Fisher, Q.J. Mudrock-hosted carbonate concretions: A review of growth mechanisms and their influence on chemical and isotopic composition. *J. Geol. Soc.* **2000**, *157*, 239–251. [[CrossRef](#)]
25. Dale, A.; John, C.M.; Mozley, P.S.; Smalley, P.C.; Muggeridge, A.H. Time-capsule concretions: Unlocking burial diagenetic processes in the Mancos Shale using carbonate clumped isotopes. *Earth Planet. Sci. Lett.* **2014**, *394*, 30–37. [[CrossRef](#)]
26. Coleman, M.L.; Raiswell, R. Sources of carbonate and origins of zonation in pyritiferous carbonate concretions: Evaluation of a dynamic model. *Am. J. Sci.* **1995**, *295*, 282–308. [[CrossRef](#)]
27. Incerpi, N.; Martire, L.; Bernasconi, S.M.; Manatschal, G.; Gerdes, A. Silica-rich septarian concretions in biogenic silica-poor sediments: A marker of hydrothermal activity at fossil hyper-extended rifted margins (Err nappe, Switzerland). *Sediment. Geol.* **2018**, *378*, 19–33. [[CrossRef](#)]
28. Dabard, M.P.; Loi, A. Environmental control on concretion-forming processes: Examples from Paleozoic terrigenous sediments of the North Gondwana margin, Armorican Massif (Middle Ordovician and Middle Devonian) and SW Sardinia (Late Ordovician). *Sediment. Geol.* **2012**, *267*, 93–103. [[CrossRef](#)]
29. Dill, H.G. Kaolin: Soil, rock and ore from the mineral to the magmatic, sedimentary and metamorphic environments. *Earth-Sci. Rev.* **2016**, *161*, 16–129. [[CrossRef](#)]
30. Ehya, F. Rare earth element and stable isotope (O, S) geochemistry of barite from the Bijgan deposit, Markazi Province, Iran. *Miner. Petrol.* **2012**, *104*, 81–93. [[CrossRef](#)]
31. Liu, H.; Tan, X.; Li, Y.; Cao, J.; Luo, B. Occurrence and conceptual sedimentary model of Cambrian gypsum-bearing evaporites in the Sichuan Basin, SW China. *Geosci. Front.* **2018**, *9*, 1179–1191. [[CrossRef](#)]
32. Bhattacharjee, P.; Goswami, S.; Bhagat, S.; Verma, M.B. Gypsum-anhydrites in 1.9 Ga Vempalle Formation, Cuddapah basin, India: A note on the Paleoproterozoic environment and diagenetic condition. *Earth Syst. Sci.* **2018**, *127*, 114. [[CrossRef](#)]
33. Clements, T.; Purnell, M.; Gabbott, S. The Mazon Creek Lagerstätte: A diverse late Paleozoic ecosystem entombed within siderite concretions. *J. Geol. Soc.* **2018**, *176*, 1–11. [[CrossRef](#)]
34. Wu, J.; Boyle, E.; Sunda, W.; Wen, L.S. Soluble and colloidal iron in the oligotrophic North Atlantic and North Pacific. *Science* **2001**, *293*, 847–849. [[CrossRef](#)]

35. Yao, C.; Ma, D.; Ding, H.; Zhang, X.; Huang, H. Trace elements and stable isotopic geochemistry of an Early Cambrian chert-phosphorite unit from the lower Yurtus Formation of the Sugetbrak section in the Tarim Basin. *Sci. China Earth Sci.* **2014**, *57*, 454–464. [[CrossRef](#)]
36. Li, M.; Chen, J.; Wang, T.; Zhong, N.; Shi, S. Nitrogen isotope and trace element composition characteristics of the Lower Cambrian Niutitang Formation shale in the upper-middle Yangtze region, South China. *Palaeogeogr. Palaeoclimatol.* **2018**, *501*, 1–12. [[CrossRef](#)]
37. Li, J.; Chen, D. Summary of quantified research method on paleosalinity. *PGRE* **2003**, *10*, 1–3, (In Chinese with English Abstract).
38. Wang, Y.; Guo, W.; Zhang, G. Application of some geochemical indicators in determining of sedimentary environment of the Funding Group (Paleogene), Jin-Hu depression, Kiangs Province. *J. Tongji Univ.* **1979**, *2*, 51–60, (In Chinese with English Abstract).
39. Wang, K.; Luo, S. Geochemical characteristics of manganese-bearing sequences of Gaoyuzhuang formation in the north Hebei depression. *Miner. Res. Geol.* **2010**, *24*, 187–192, (In Chinese with English Abstract).
40. Weyer, S.; Münker, C.; Mezger, K. Nb/Ta, Zr/Hf and REE in the depleted mantle: Implications for the differentiation history of the crust-mantle system. *Earth Planet Sci. Lett.* **2003**, *205*, 309–324. [[CrossRef](#)]
41. Bau, M.; Koschinsky, A. Hafnium and neodymium isotopes in seawater and in ferromanganese crusts: The “element perspective”. *Earth Planet. Sci. Lett.* **2006**, *241*, 952–961. [[CrossRef](#)]
42. Schmidt, K.; Bau, M.; Hein, J.R.; Koschinsky, A. Fractionation of the geochemical twins Zr–Hf and Nb–Ta during scavenging from seawater by hydrogenetic ferromanganese crusts. *Geochim. Cosmochim. Acta* **2014**, *140*, 468–487. [[CrossRef](#)]
43. Zhao, Z. *Geochemical Principles of Trace Element*; Science Press: Beijing, China, 2016; ISBN 978-7-03-047496-4.
44. Zhang, T.; Trela, W.; Jiang, S.; Nielsen, J.K.; Shen, Y. Major oceanic redox condition change correlated with the rebound of marine animal diversity during the Late Ordovician. *Geology* **2011**, *39*, 675–678. [[CrossRef](#)]
45. Thiel, V.; Hoppert, M. Fatty acids and other biomarkers in two Early Jurassic concretions and their immediate host rocks (Lias delta, Buttenheim clay pit, Bavaria, Germany). *Org. Geochem.* **2018**, *120*, 42–45. [[CrossRef](#)]
46. Grice, K.; Holman, A.I.; Plet, C.; Tripp, M. Fossilized Biomolecules and Biomarkers in Carbonate Concretions from Konservat-Lagerstätten. *Minerals* **2019**, *9*, 158. [[CrossRef](#)]
47. Schulz, H. *Quantification of Early Diagenesis: Dissolved Constituents in Pore Water and Signals in the Solid Marine Geochemistry*; Springer: Berlin, Germany, 2000; pp. 73–124.
48. Chan, M.A.; Ormö, J.; Park, A.J.; Stich, M.; Souza-Egipsy, V.; Komatsu, G. Models of iron oxide concretion formation: Field, numerical, and laboratory comparisons. *Geofluids* **2007**, *7*, 356–368. [[CrossRef](#)]



© 2019 by the authors. Licensee MDPI, Basel, Switzerland. This article is an open access article distributed under the terms and conditions of the Creative Commons Attribution (CC BY) license (<http://creativecommons.org/licenses/by/4.0/>).